Supplementary Information for

Unconventional bound states in the continuum from metamaterial induced electron acoustic waves

Wenhui Wang[1,*], Antonio Günzler[1], Bodo D. Wilts[1], Ullrich Steiner[1], Matthias Saba[1,†], Wenhui Wang[a,*], Antonio Günzler[a], Bodo D. Wilts[a,b], Ullrich Steiner[a], and Matthias Saba[a,*]

[1]Adolphe Merkle Institute, University of Fribourg, Chemin des Verdiers 4, 1700 Fribourg, Switzerland.
[a]Adolphe Merkle Institute, University of Fribourg, Chemin des Verdiers 4, 1700 Fribourg, Switzerland.
[b]Department of Chemistry and Physics of Materials, University of Salzburg, Jakob-Haringer-Straße 2A, 5020 Salzburg, Austria.
Email: *wenhui.wang@unifr.ch, *matthias.saba@unifr.ch

S1 Plasma and metallic-network meta-material modes

S1.1 Single plasma fluid model

We begin with a single plasma fluid model for an ideal warm plasma [61]. This model consists of a set of three equations describing the charge carrier (CC) dynamics,

$$\frac{\partial n}{\partial t} + \nabla \cdot (n\mathbf{u}) = 0 \tag{S1a}$$

$$m\left(\frac{\partial\, n\mathbf{u}}{\partial t} + \nabla \cdot [n\mathbf{u} \otimes \mathbf{u}]\right) = -\nabla P + \rho\mathbf{E} \tag{S1b}$$

$$\frac{\mathrm{d}}{\mathrm{d}t}\left(Pn^{-\gamma}\right) = 0\,. \tag{S1c}$$

Eq. (S1a) is the continuity equation of CC conservation, where $n(\mathbf{r},t)$ is the CC volume density field and $\mathbf{u}(\mathbf{r},t)$ is the CC velocity field. Eq. (S1b) is the Navier-Stokes equation for the electrically excited CC liquid, where we ignore shear forces, the non-linear magnetic field contribution in the Lorentz force density, and gravitational contributions. In this equation, $\otimes$ is the outer product, m the effective mass of the charge carriers, $P(\mathbf{r},t)$ the CC liquid pressure field, and $\rho(\mathbf{r},t) := qn(\mathbf{r},t)$ the CC charge density. We note that a kinetic pressure term is present in any liquid. Here, P should be understood as the total mesoscopic pressure based on the microscopic statistical ensemble of CCs, including inter-particle Coulomb interactions. Finally, Eq. (S1c) is a local adiabatic equation with the adiabatic index γ, which can be rigorously derived from an energy balance equation in the limit where the flow velocity is much larger than vicious and thermal diffusion velocities. These fluid equations are closed with the Maxwell curl equations, which describe the electromagnetic field dynamics. In Lorentz-Heaviside units,

$$\nabla \times \mathbf{E} = -\frac{1}{c}\frac{\partial \mathbf{H}}{\partial t} \tag{S2a}$$

$$\nabla \times \mathbf{H} = \frac{1}{c}\left(\frac{\partial \mathbf{E}}{\partial t} + \mathbf{j}\right)\,, \tag{S2b}$$

with $\mathbf{E}(\mathbf{r},t)$ and $\mathbf{H}(\mathbf{r},t)$ the electric and magnetic fields, respectively, c the speed of light in vacuum, and $\mathbf{j}(\mathbf{r},t) := \rho(\mathbf{r},t)\mathbf{u}(\mathbf{r},t)$ the current density of the plasma charge carriers.

We now linearize Eq. (S1) assuming small variations in the density and pressure

$$n(\mathbf{r},t) := n_0 + \delta n(\mathbf{r},t)$$
$$P(\mathbf{r},t) := P_0 + \delta P(\mathbf{r},t)$$

and thus small velocities $\mathbf{u}(\mathbf{r},t)$ to arrive at

$$\frac{\partial \delta n}{\partial t} + n_0 \nabla \cdot \mathbf{u} = 0 \tag{S3a}$$
$$m\, n_0 \frac{\partial\, \mathbf{u}}{\partial t} = -\nabla \delta P + \rho \mathbf{E} \tag{S3b}$$
$$\frac{\mathrm{d}}{\mathrm{d}t}\left(\delta P - \gamma \frac{P_0}{n_0}\delta n\right) = 0\ . \tag{S3c}$$

Since $\delta P = 0$ if $\delta n = 0$, Eq. (S3c) is solved by $\delta P = \gamma P_0\, \delta n / n_0$. Finally, since Eq. (S2) and Eq. (S3) are now both spatiotemporally homogeneous and linear in all fields, we can make a plane wave ansatz $n(\mathbf{r},t) := n \exp\{\imath(\mathbf{k}\cdot\mathbf{r} - \omega t)\}$, *etc.*, such that the field symbols represent their constant coefficients from this point on to obtain

$$c\,\mathbf{k} \times \mathbf{E} = \omega \mathbf{H} \tag{S4a}$$
$$-c\,\mathbf{k} \times \mathbf{H} = \omega \mathbf{E} + \imath \mathbf{j} \tag{S4b}$$
$$\omega \delta n = n_0 \mathbf{k} \cdot \mathbf{u} \tag{S4c}$$
$$\omega m n_0 \mathbf{u} = -\mathbf{k}\,\frac{\gamma P_0}{n_0}\delta n + \imath q n_0 \mathbf{E}\ . \tag{S4d}$$

We now introduce the plasma frequency $\omega_\mathrm{p}^2 := n_0 q^2/m$, the plasma wave number $k_\mathrm{p} := \omega_\mathrm{p}/c$, and the dimensionless pressure parameter $\kappa^2 := \gamma P_0/(n_0 m c^2)$, to obtain a $\mathbf{k}$-family of linear Hermitian eigenproblems

$$\mathcal{H}(\mathbf{k})\,\mathbf{v} = \frac{\omega}{\omega_\mathrm{p}}\,\mathbf{v} \tag{S5}$$

for the eigenvalue ω/ω_p. The eigenvector is defined as

$$\mathbf{v} := \begin{pmatrix} \mathbf{E} \\ \mathbf{H} \\ \frac{\kappa}{k_\mathrm{p}} q\, \delta n \\ \frac{1}{\omega_\mathrm{p}} \mathbf{j} \end{pmatrix}\ .$$

The dimensionless matrix operator

$$\mathcal{H} := \begin{pmatrix} \mathcal{H}_\mathrm{field} & \mathcal{H}_\mathrm{int} \\ \mathcal{H}_\mathrm{int}^\dagger & \mathcal{H}_\mathrm{fluid} \end{pmatrix}\ , \tag{S6}$$

which we from now on refer to as Hamiltonian, has the sub-blocks

$$\mathcal{H}_\mathrm{field} := \frac{1}{\imath k_\mathrm{p}} \sigma_y \otimes \underline{\underline{\mathbf{K}}}_\times\ ,\ \mathcal{H}_\mathrm{int} := \begin{pmatrix} 1 \\ 0 \end{pmatrix} \otimes \begin{pmatrix} \mathbf{0} & -\imath \mathbb{1}_3 \end{pmatrix}\ ,\ \text{and}\ \mathcal{H}_\mathrm{fluid} := \frac{\kappa}{k_\mathrm{p}} \begin{pmatrix} 0 & \mathbf{k}^\dagger \\ \mathbf{k} & \underline{\underline{\mathbf{0}}} \end{pmatrix}\ .$$

Here, we have used the Pauli spin matrix σ_y, the vector product matrix $\underline{\underline{\mathbf{K}}}_\times \mathbf{w} := \mathbf{k} \times \mathbf{w}$, the Kronecker (tensor) product $\otimes$, the zero vector $\mathbf{0}$ and matrix $\underline{\underline{\mathbf{0}}}$ of dimension 3, and the identity matrix $\mathbb{1}_d$ of dimension d; $\underline{\underline{\mathbf{A}}}^\dagger$ denotes the Hermitian adjoint of $\underline{\underline{\mathbf{A}}}$.

The problem is, of course, isotropic so that we can choose the coordinate frame such that $\mathbf{k} = k\,\mathbf{e}_z$ without loss of generality. The eigenproblem Eq. (S5) predicts a four-fold degenerate zero-frequency band $\omega(k) = 0$. The associated eigenspace is spanned by two spurious longitudinal modes, which violate the Maxwell divergence equations, and the static magnetic field solutions generated by a transverse current density

$$\begin{pmatrix} H_x \\ H_y \end{pmatrix} = -\frac{k_\mathrm{p}}{k} \sigma_y \begin{pmatrix} j_x \\ j_y \end{pmatrix}$$

at constant charge $\delta_n = 0$ and vanishing electric field.

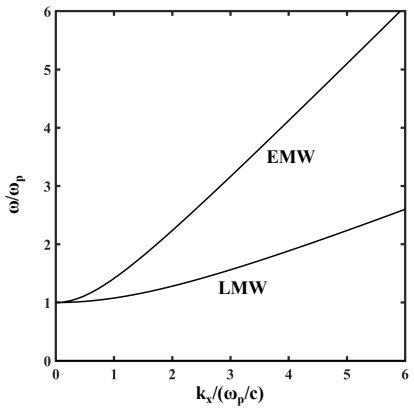

Fig. S 1: Dispersion relation of a single plasma fluid with thermal coefficient $\kappa = 0.4$. It has a longitudinal Langmuir (LMW) and a doubly-degenerate electromagnetic wave (EMW) band.

Note that the system is particle-hole symmetric [62], that is, for every eigenvector $\mathbf{v}$ of $H(k)$ with energy ω, there is one particle-hole symmetric eigenvector $\mathbf{v}^*$ with energy $-\omega$. Thus we show only the positive frequency bands in Fig. S1. They follow the longitudinal mode Langmuir dispersion[1]

$$\frac{\omega_l}{\omega_p} = \sqrt{1 + \left(\frac{\kappa k_l}{k_\mathrm{p}}\right)^2} \tag{S7}$$

with fields $\mathbf{E} = \mathbf{e}_z$, $\mathbf{H} = 0$, $\delta n = \frac{\imath k_l}{q}$, and $\mathbf{j} = \imath\omega_l \mathbf{e}_z$; and the two-fold degenerate transverse light mode dispersion

$$\frac{\omega_t}{\omega_p} = \sqrt{1 + \left(\frac{k_t}{k_\mathrm{p}}\right)^2} \tag{S8}$$

with fields $\mathbf{E}_\pm = \mathbf{e}_x \pm \imath \mathbf{e}_y$, $\mathbf{H}_\pm = \frac{ck_t}{\omega_t}\left(\mathbf{e}_y \mp \imath \mathbf{e}_x\right)$, $\delta n = 0$, and $\mathbf{j} = \frac{2\imath\omega_p^2}{\omega_t}\mathbf{E}_\pm$.

S1.2 Metallic network metamaterial modes

At low frequencies in the microwave regime, metals act like perfect electrical conductors (PECs), which do not support propagating modes in the bulk. We can reduce the CC density by employing plasmonic metal wires to introduce an effective plasma frequency for excitations in the wire direction while maintaining the lossless PEC character . A 3D metallic pcu [64] wire-mesh with sub-wavelength period therefore effectively generates a lossless plasma at microwave excitations. Based on [38], we here formally show that the electro-dynamic theory of the metallic pcu network in the long wavelength limit is indeed equivalent to the single plasma model with a constant pressure parameter $\kappa = 1/\sqrt{3}$.

We use the macroscopic constitutive relations from [38] that have been derived for a square lattice of aligned wires (along $\mathbf{e}_z$) in the homogenization picture. We start with the current $I(z)$ and the electric potential $V(z)$ between neighbouring wires. A comparison of the magnetic flux through a rectangle of infinitesimal height with the corresponding boundary integral (Ampére's law in integral form) yields (assuming a plane wave form)[2]

$$k_z V = \omega L I - \imath \langle E_z \rangle, \tag{S9}$$

with the self-inductance per unit length of the wires in the mesh $L = \frac{1}{2\pi c^2}\log\left(\frac{a^2}{4r(a-r)}\right)$ that is a simple consequence of the Biot-Savart law for the individual wires and only depends on the lattice constant (nearest neighbour distance) a and the wire radius r. The potential between neighbouring wires is, on the other hand related to the linear charge density $\lambda(z)$ via the linear relation $\lambda = CV$ with

[1] Note that we do not normalize fields and choose the electric and magnetic field without dimension (instead of their standard cgs unit $\mathrm{g}^{1/2}\mathrm{cm}^{-1/2}\mathrm{s}^{-1}$) here for convenience.

[2] Note that we here use the physics convention for the monochromatic ansatz $\exp\{-\imath\omega t\}$ and Lorentz-Heaviside units in contrast to [63].

the effective capacitance per unit length $C = 1/(c^2 L)$ that is obtained using Gauss' law. Combining this relation with charge conservation $k_z I = \omega\lambda$ leads to

$$k_z I = \omega C V. \tag{S10}$$

Eq. (S9) and Eq. (S10) can be readily generalized to a 3D connected pcu wire-mesh: Eq. (S9) simply acquires full vector form with $k_z \mapsto \mathbf{k}$, $I \mapsto a^2\langle\mathbf{j}\rangle$, and $\langle E_z\rangle \mapsto \langle\mathbf{E}\rangle$. A factor of $1/3$ effectively reduces the linear charge density as the charges spread over three wires in each direction in the unit cell, and the pcu network is fully connected. A more rigorous treatment for wires of finite radius reveals that this factor is indeed better approximated by [54]

$$\kappa^2 = \frac{1 + 2\frac{k_\mathrm{p}^2}{k_1^2}}{3}\ , \tag{S11a}$$

$$\text{with the plasma wavenumber } \frac{k_\mathrm{p} a}{2\pi} = \left[\sum_{(m,n)\in\mathbb{N}^2\setminus(0,0)} \frac{J_0^2\left(\frac{2\pi r}{a}\sqrt{m^2+n^2}\right)}{m^2+n^2}\right]^{(-1/2)}\ , \tag{S11b}$$

$$\text{and } \frac{k_1 a}{2\pi} = \left[\sum_{m\in\mathbb{N}\setminus 0} \frac{J_0^2\left(\frac{2\pi r}{a} m\right)}{m^2}\right]^{(-1/2)}\ . \tag{S11c}$$

In practice, the wire-mesh pressure parameter falls in a range between $\kappa \approx 2/3$ for a wire radius of $r = a/100$ and $\kappa \approx 3/4$ for $r = a/5$. Rearranging, we obtain

$$\imath\langle\mathbf{E}\rangle + \mathbf{k}V = \omega a^2 L\langle\mathbf{j}\rangle \tag{S12a}$$

$$\kappa^2 a^2 \mathbf{k}\cdot\langle\mathbf{j}\rangle = \omega C V\ . \tag{S12b}$$

Defining the plasma frequency as the cut-off frequency of the aligned wire mesh [37] $k_\mathrm{p}^2 a^2 := C$, which is indeed a good approximation of the definition in Eq. (S11b), and the field vector

$$\mathbf{v} := \begin{pmatrix} \langle\mathbf{E}\rangle \\ \langle\mathbf{H}\rangle \\ \frac{\kappa}{k_\mathrm{p}} V \\ \langle\mathbf{j}\rangle/\omega_p \end{pmatrix}\ ,$$

we formally arrive at the above eigenproblem Eq. (S5) with a κ that is confined in a small interval and only weakly depends on the geometrical parameters of the wire-mesh. We finally note that the scaled potential $\frac{\kappa}{k_\mathrm{p}} V$ equals the scaled CC density $\frac{\kappa}{k_\mathrm{p}} q\delta n$ from Sec. (S1.1) if we associate the linear charge density along the PEC wires per unit cell area λ/a^2 with the charge density ρ of the plasma, so that the field vector $\mathbf{v}$ is identical in both models. Fig. S2 shows the bandstructure obtained through a full-wave simulation, which agrees well with the single plasma fluid model shown in Fig. S1. The two modes in Fig. S2(b) correspond to the longitudinal (LMW) and transverse (EMW) modes in Fig. S1.

S1.3 Hydrodynamical double plasma fluid model

We now consider a plasma consisting of two CC species of respective charge q_i, mass m_i, and equilibrium CC density $n_0^{(i)}$ and pressure $P_0^{(i)}$ $(i = 1, 2)$. The associated plasma frequencies, plasma wave numbers, and pressure parameters are $\omega_{\mathrm{p}i}$, $k_{\mathrm{p}i}$, and κ_i. We further assume that CC interact only amongst their own species, which is physically, of course, only possible in a universe where particles of a different type do not interact (via Coulomb forces or otherwise). The theory is, however, approximately valid if the interaction is weak or if the two charge carriers are separated on a mesoscopic scale.

In the prescribed situation, the corresponding fluid equations Eq. (S4c) and Eq. (S4d) separate into two individual equations, while both current densities contribute to the Ampère-Maxwell law

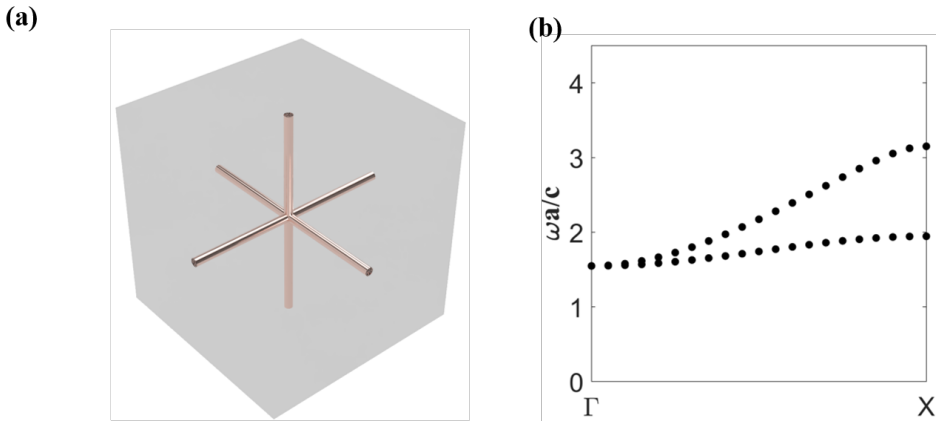

Fig. S2: (a) Single metallic wire-mesh with radius $r = 0.02a$. (b) Dispersion relation of (a).

Eq. (S4b),

$$c\,\mathbf{k}\times\mathbf{E} = \omega\mathbf{H} \tag{S13a}$$

$$-c\,\mathbf{k}\times\mathbf{H} = \omega\mathbf{E} + \imath\sum_{i=1}^{2}\mathbf{j_i} \tag{S13b}$$

$$\omega\delta n_i = n_0^{(i)}\mathbf{k}\cdot\mathbf{u}_i \quad (i=1,2) \tag{S13c}$$

$$\omega m_i n_0^{(i)}\mathbf{u}_i = -\mathbf{k}\,\frac{\gamma P_0^{(i)}}{n_0^{(i)}}\delta n_i + \imath q_i n_0^{(i)}\mathbf{E} \quad (i=1,2)\ . \tag{S13d}$$

In the context of our analysis, we are examining a broader scenario where the plasma frequency of the two distinct electron species is not equal. Specifically, we are making the assumption that ω_{p1} and ω_{p2} are different, with real quotient $m = \frac{\omega_{p2}}{\omega_{p1}}$. As demonstrated in Sec. (S1.1), we can express the Hamiltonian for HDP in the following form:

$$\mathcal{H}_{\rm HDP}(\mathbf{k})\,\mathbf{v}_{\rm HDP} = \frac{\omega}{c}\,\mathbf{v}_{\rm HDP} \tag{S14}$$

where

$$\mathcal{H}_{\rm HDP} := \begin{pmatrix} \mathcal{H}^{\rm HDP}_{\rm field} & \mathcal{H}^{\rm HDP}_{\rm int} \\ (\mathcal{H}^{\rm HDP}_{\rm int})^{\dagger} & \mathcal{H}^{\rm HDP}_{\rm fluid} \end{pmatrix}\ , \tag{S15}$$

with the sub-blocks

$$\mathcal{H}^{\rm HDP}_{\rm field} := -\imath\sigma_y \otimes \frac{\underline{\underline{\mathbf{K}}}}{k_{p1}}, \mathcal{H}^{\rm HDP}_{\rm int} := -\imath \begin{pmatrix} 1 & m \end{pmatrix} \otimes \begin{pmatrix} 1 \\ 0 \end{pmatrix} \otimes \begin{pmatrix} \mathbf{0} & \mathbb{1}_3 \end{pmatrix}$$

and

$$\mathcal{H}^{\rm HDP}_{\rm fluid} := \begin{pmatrix} \kappa_1 & 0 \\ 0 & \kappa_2 \end{pmatrix} \otimes \begin{pmatrix} 0 & \mathbf{k}^{\dagger} \\ \mathbf{k} & \underline{\underline{\mathbf{0}}} \end{pmatrix}\ .$$

In analogy to Sec. (S1.1), the eigenvector can be defined as

$$\mathbf{v} := \begin{pmatrix} \mathbf{E} \\ \mathbf{H} \\ \frac{\kappa_1}{k_{\rm p1}} q\,\delta n_1 \\ \frac{1}{\omega_{\rm p1}}\mathbf{j_1} \\ \frac{\kappa_2}{k_{\rm p2}} q\,\delta n_2 \\ \frac{1}{\omega_{\rm p2}}\mathbf{j_2} \end{pmatrix}\ .$$

Similar to the single plasma, the HDP Hamiltonian yields an EAW and a Langmuir band. The dispersion of the transverse band and Langmuir band can be expressed as

$$\frac{\omega_t}{c} = \sqrt{k_{\rm p1}^2 + k_{\rm p2}^2 + k_t^2} \tag{S16}$$

$$\frac{\omega_l}{c} \approx \sqrt{k_{\mathrm{p1}}^2 + k_{\mathrm{p2}}^2 + \left[1 + 2\frac{k_{\mathrm{p2}}^2 - k_{\mathrm{p1}}^2}{k_{\mathrm{p2}}^2 + k_{\mathrm{p1}}^2}\frac{\kappa_2 - \kappa_1}{\kappa_2 + \kappa_1}\right]\kappa^2\, k_l^2} \tag{S17}$$

Apart from the previously mentioned modes, an additional mode called the electron acoustic wave (EAWs) is found, which extends from zero frequency to the double plasma effective plasma frequency at $\sqrt{k_{\mathrm{p1}}^2 + k_{\mathrm{p2}}^2}$. The eigenproblem Eq. (S14) can be solved algebraically by employing any standard computer algebra tool. However, a more convenient and elegant manual solution can be obtained using the $\mathbf{k}\cdot\mathbf{p}$ perturbation theory at the Γ-point. It is worth noting that this method is precise when used to analyze the EAW band, as demonstrated below.

The general approach [48]can be briefly summarized as follows: First, we expand the eigenstates at a specific $\mathbf{k}=\mathbf{k}_0+\delta\mathbf{k}$ (where $\mathbf{k}_0=0$ at the Γ-point) in reciprocal space using the basis of eigenstates at $\mathbf{k}_0$, with $\delta\mathbf{k}$ having infinitesimal length. Assuming that the solution of the Hamiltonian at $\mathbf{k}_0$ is known for the eigenspace $\mathcal{U}$ associated with a particular eigenvalue $\lambda_0 := \omega(k_0)/c$, we define the orthonormalized eigenvectors $\mathbf{u}_\alpha$ that span $\mathcal{U}$ as follows:

$$\mathcal{H}(\mathbf{k}_0)\mathbf{u}_\alpha = \lambda_0\mathbf{u}_\alpha \ .$$

If the components of the Hamiltonian are analytical at $\mathbf{k}_0$, we obtain in first order in $\delta\mathbf{k}$,

$$\mathcal{H}(\mathbf{k}_0+\delta\mathbf{k}) = \mathcal{H}(\mathbf{k}_0) + \underbrace{\delta\mathbf{k}\cdot\left[\nabla_{\mathbf{k}}\mathcal{H}\right](\mathbf{k}_0)}_{=:\,\delta\mathcal{H}} \ .$$

At the perturbed point $\mathbf{k}_0+\delta\mathbf{k}$, the eigenvectors $\mathbf{v}_n$ are an element of $\mathcal{U}$ in zero order perturbation theory. This immediately yields the identity (using Einstein notation),

$$\mathbf{v}_n = (\mathbf{u}_\alpha\cdot\mathbf{v}_n)\,\mathbf{u}_\alpha := c_\alpha^{(n)}\,\mathbf{u}_\alpha \ .$$

As a result, the eigenvalue equation at $\mathbf{k}_0+\delta\mathbf{k}$ becomes

$$\left[\lambda_0 + \delta\mathcal{H}\right] c_\alpha^{(n)}\mathbf{u}_\alpha = \lambda_n c_\alpha^{(n)}\mathbf{u}_\alpha \ .$$

Upon testing with $\mathbf{u}_\alpha$, we obtain its weak form, which is an algebraic eigenvalue equation that has the dimension of $\mathcal{U}$,

$$\underbrace{\mathbf{u}_\alpha\cdot(\delta\mathcal{H}\mathbf{u}_\beta)}_{=:\,\mathcal{H}_{\alpha\beta}}\, c_\alpha^{(n)} = (\lambda_n - \lambda_0)\, c_\alpha^{(n)} \ . \tag{S18}$$

In other words, the deviation of the $\dim(\mathcal{U})$ eigenvalues λ_n from λ_0 is given by the eigenvalues of the effective Hamiltonian $\mathcal{H}_{\alpha\beta}$, whose entries are the matrix elements of the first order perturbation $\delta\mathcal{H}$ in $\mathcal{U}$.

Since $\mathcal{H}$ is linear in $\mathbf{k}$ for the HDP Hamiltonian Eq. (S15), the first order expansion is exact, that is $\mathcal{H}_{\mathrm{HDP}} = \mathcal{H}_0 + \delta\mathcal{H}$ with

$$\mathcal{H}_0 = \begin{pmatrix} \underline{\underline{\mathbf{0}}} & \mathcal{H}_{\mathrm{int}} \\ \mathcal{H}_{\mathrm{int}}^\dagger & \underline{\underline{\mathbf{0}}} \end{pmatrix}$$

$$\text{and} \quad \delta\mathcal{H} = \begin{pmatrix} \mathcal{H}_{\mathrm{field}}(\delta\mathbf{k}) & \underline{\underline{\mathbf{0}}} \\ \underline{\underline{\mathbf{0}}} & \mathcal{H}_{\mathrm{fluid}}(\delta\mathbf{k}) \end{pmatrix} \ .$$

Since we are interested in the eigenspace of $\mathcal{H}_0$ at vanishing frequency, we are searching for its kernel, which is 8-dimensional and contains arbitrary $\mathbf{H}$, arbitrary V_1 or V_2, and arbitrary $\mathbf{j}_1 = -\mathbf{j}_2$, with all other fields vanishing. Labelling the field components in $\mathbf{u}_\alpha$ with i and disregarding the trivial electrostatic solution with $\mathbf{H} \neq 0$, we thus obtain the 5-dimensional eigenspace matrix with

orthogonormalized eigenvectors as rows

$$U_{i\alpha}=\frac{1}{\sqrt{k_{\mathrm{p1}}^2+k_{\mathrm{p2}}^2}}\begin{pmatrix}0&0&0&0&0\\0&0&0&0&0\\0&0&0&0&0\\0&0&0&0&0\\0&0&0&0&0\\0&0&0&0&0\\\sqrt{k_{\mathrm{p1}}^2+k_{\mathrm{p2}}^2}&0&0&0&0\\0&0&k_{\mathrm{p2}}&0&0\\0&0&0&k_{\mathrm{p2}}&0\\0&0&0&0&k_{\mathrm{p2}}\\0&\sqrt{k_{\mathrm{p1}}^2+k_{\mathrm{p2}}^2}&0&0&0\\0&0&-k_{\mathrm{p1}}&0&0\\0&0&0&-k_{\mathrm{p1}}&0\\0&0&0&0&-k_{\mathrm{p1}}\end{pmatrix}.$$

The effective Hamiltonian is thus

$$\mathcal{H}_{\alpha\beta}=U_{i\alpha}\delta\mathcal{H}_{ij}U_{j\beta}=\begin{bmatrix}0&\underline{\underline{\mathbf{h}}}\\\underline{\underline{\mathbf{h}}}^{\intercal}&0\end{bmatrix},\tag{S19}$$

where

$$\underline{\underline{\mathbf{h}}}=\frac{1}{\sqrt{m^2+1}}\begin{bmatrix}\kappa_1k_xm&\kappa_1k_ym&\kappa_1k_zm\\\kappa_2k_x&\kappa_2k_y&\kappa_2k_z\end{bmatrix}.$$

Three of the eigenvalues of the perturbation Hamiltonian in Eq. (S19) are zero. In addition, we reproduce the EAW band in Eq. (S1.3) and its chirally symmetry counterpart:

$$\omega_a{}^2=\frac{m^2+\frac{\kappa_2{}^2}{\kappa_1{}^2}}{m^2+1}\kappa_1{}^2c^2k_a{}^2,$$

A noteworthy observation is that as κ_1 approaches κ_2, the slope of the EAW is only minimally affected by changes in the plasma frequencies. This is particularly evident when κ_1 equals κ_2, in which case the dispersion relationship can be represented as $\lambda=\kappa_1 ck_a$, and is independent of the plasma frequency.

S1.4 Plasmonic double net metamaterials

As we have shown in Sec. (S1.2), a PEC pcu wire-mesh acts like a single plasma in the homogenization regime, that is, if the Bloch wavevector of the mode satisfies $|\mathbf{k}|\ll 2\pi/a$. We use the parameter vector $P:=(r_1/a,r_2/a,R)$ to define a pcu double network, where r_i are the individual network radii, a the cubic lattice constant, and R is the offset in each Cartesian direction so that the two networks are separated by a shift vector $\mathbf{S}:=(1,1,1)^{\intercal}R$. Assuming that the networks are well separated, the DNM fields, therefore, obey Eq. (S13) with the substitutions discussed in Sec. (S1.2).

The two networks generally exhibit different plasma frequencies $\omega_{\mathrm{p}i}$ that depend on r_i and lie approximately between $k_{\mathrm{p}}a/(2\pi)=1/5$ for $r=1/100$ and $k_{\mathrm{p}}(2\pi)=3/5$ for $r=1/5$. The pressure parameters are generally also different, but contained in a very small interval between $\kappa=2/3$ and $\kappa=3/4$, so that it is useful to introduce $\kappa_1:=\kappa-\delta\kappa$ and $\kappa_2:=\kappa+\delta\kappa$ with $\delta\kappa\ll\kappa$. The canonical field vector of the double wire mesh is, therefore

$$\mathbf{v}_{\mathrm{DN}}:=\begin{pmatrix}\langle\mathbf{E}\rangle\\\langle\mathbf{H}\rangle\\\frac{\kappa-\delta\kappa}{k_{\mathrm{p1}}}V_1\\\langle\mathbf{j}_1\rangle\\\frac{\kappa+\delta\kappa}{k_{\mathrm{p2}}}V_2\\\langle\mathbf{j}_2\rangle\end{pmatrix}.$$

The eigenproblem can be written as

$$\mathcal{H}_{\mathrm{DN}}(\mathbf{k})\,\mathbf{v}_{\mathrm{DN}} = \frac{\omega}{c}\,\mathbf{v}_{\mathrm{DN}} \tag{S20}$$

with the associated Hamiltonian

$$\mathcal{H}_{\mathrm{DN}} := \begin{pmatrix} \mathcal{H}^{\mathrm{DN}}_{\mathrm{field}} & \mathcal{H}^{\mathrm{DN}}_{\mathrm{int}} \\ \left(\mathcal{H}^{\mathrm{DN}}_{\mathrm{int}}\right)^{\dagger} & \mathcal{H}^{\mathrm{DN}}_{\mathrm{fluid}} \end{pmatrix} , \tag{S21}$$

with the sub-blocks

$$\mathcal{H}^{\mathrm{DN}}_{\mathrm{field}} := -\imath\sigma_y \otimes \underline{\underline{\mathbf{K}}}_{\times},\ \mathcal{H}^{\mathrm{DN}}_{\mathrm{int}} := -\imath \begin{pmatrix} k_{\mathrm{p1}} & k_{\mathrm{p2}} \end{pmatrix} \otimes \begin{pmatrix} 1 \\ 0 \end{pmatrix} \otimes \begin{pmatrix} \mathbf{0} & \mathbb{1}_3 \end{pmatrix}$$

and

$$\mathcal{H}^{\mathrm{DN}}_{\mathrm{fluid}} := \begin{pmatrix} \kappa-\delta\kappa & 0 \\ 0 & \kappa+\delta\kappa \end{pmatrix} \otimes \begin{pmatrix} 0 & \mathbf{k}^{\dagger} \\ \mathbf{k} & \underline{\underline{\mathbf{0}}} \end{pmatrix} .$$

With $\mathbf{k} = k\mathbf{e}_z$ w.l.o.g. because of the isotropy of the problem, this double-net eigenproblem yields the longitudinal band

$$\frac{\omega_l}{c} \approx \sqrt{k^2_{\mathrm{p1}} + k^2_{\mathrm{p2}} + \left[1 + 2\frac{k^2_{\mathrm{p2}} - k^2_{\mathrm{p1}}}{k^2_{\mathrm{p2}} + k^2_{\mathrm{p1}}}\frac{\delta\kappa}{\kappa}\right]\kappa^2\,k_l^2} \tag{S22}$$

with fields $\mathbf{E} \parallel \mathbf{e}_z$, $\mathbf{H} = 0$, and $\mathbf{j}_i =\parallel \mathbf{e}_z$; and the two-fold degenerate transverse light band

$$\frac{\omega_t}{c} = \sqrt{k^2_{\mathrm{p1}} + k^2_{\mathrm{p2}} + k_t^2} \tag{S23}$$

with $\mathbf{E}_{\pm} = \frac{\omega_t}{c}\left(\mathbf{e}_x \pm \imath\mathbf{e}_y\right)$, $\mathbf{H}_{\pm} = k_t\left(\mathbf{e}_y \mp \imath\mathbf{e}_x\right)$, $V_{i\pm} = 0$, and $\mathbf{j}_{i\pm} = \imath k_{\mathrm{p}i}\left(\mathbf{e}_x \pm \imath\mathbf{e}_y\right)$. Similar to Sec. (S1.1), the zero-frequency band is 6-fold degenerate, with two spurious longitudinal solutions and now four transverse current modes with

$$\begin{pmatrix} H_x \\ H_y \end{pmatrix} = -\frac{k_{\mathrm{p}i}}{k}\sigma_y \begin{pmatrix} j_{ix} \\ j_{iy} \end{pmatrix} \tag{S24}$$

and all other fields are vanishing.

Importantly, a new fundamental band appears below the plasma frequency. It emanates at the Γ-point at $\omega = 0$ with a constant slope as shown in the main manuscript in Figure 1(b). The associated modes are reminiscent of acoustic waves in a conventional fluid but with two species of charges fluctuating in opposite directions. The dispersion relation is

$$\frac{\omega_a}{c} \approx \left(\kappa + \frac{k^2_{\mathrm{p1}} - k^2_{\mathrm{p2}}}{k^2_{\mathrm{p1}} + k^2_{\mathrm{p2}}}\delta\kappa\right) k_a, \tag{S25}$$

with fields (in leading order in $\delta\kappa$) $\mathbf{E} = \delta\kappa k\mathbf{e}_z$, $\mathbf{H} = 0$, $V_i = -\imath\kappa(-1)^i(k^2_{\mathrm{p1}}+k^2_{\mathrm{p2}})/(4k^2_{\mathrm{p}i})$ and $\mathbf{j}_i = \frac{k_{\mathrm{p1}}}{\kappa}V_i\mathbf{e}_z$. As we can see, the magnetic field of the EAW is strictly zero, while the electric field is longitudinal and linearly depends on both $\delta\kappa$ and k. In the real DNM structures, since the HDP model is only approximately valid, the electric field of the low-frequency mode obtains an additional longitudinal term that is zero order in $\delta\kappa$ and quadratic in k. We demonstrate this behavior in the main text Fig. 2(a), by averaging the fields obtained through full-wave simulations for three different DNM geometries. The x-component increases quadratically when moving away from the Γ-point by $\mathbf{k} \parallel \mathbf{e}_x$ in all the three different DNM geometries, while the y and z components vanish. Typically, the additional linear dependence on $\delta\kappa/\kappa$ is negligible and can be disregarded. For example, if $P = (0.4, 0.1, \frac{a}{2})$, the ratio is $\delta\kappa/\kappa \approx 0.03$.

The slope of the EAW band only weakly depends on the difference in plasma frequencies of the two networks in first order $\delta\kappa$. Moreover, in DNMs, the accumulation of current in each metal network is evenly distributed into three parts along the x, y, and z directions due to the perpendicular intersection of metal lines at the nodes. This results in $\delta\kappa = 0$, which is why the slope of the EAW band is predominantly determined by the pressure parameter κ alone. Additionally, it is worth noting that the dispersion of the EAW band in the low-frequency limit remains robust against changes in

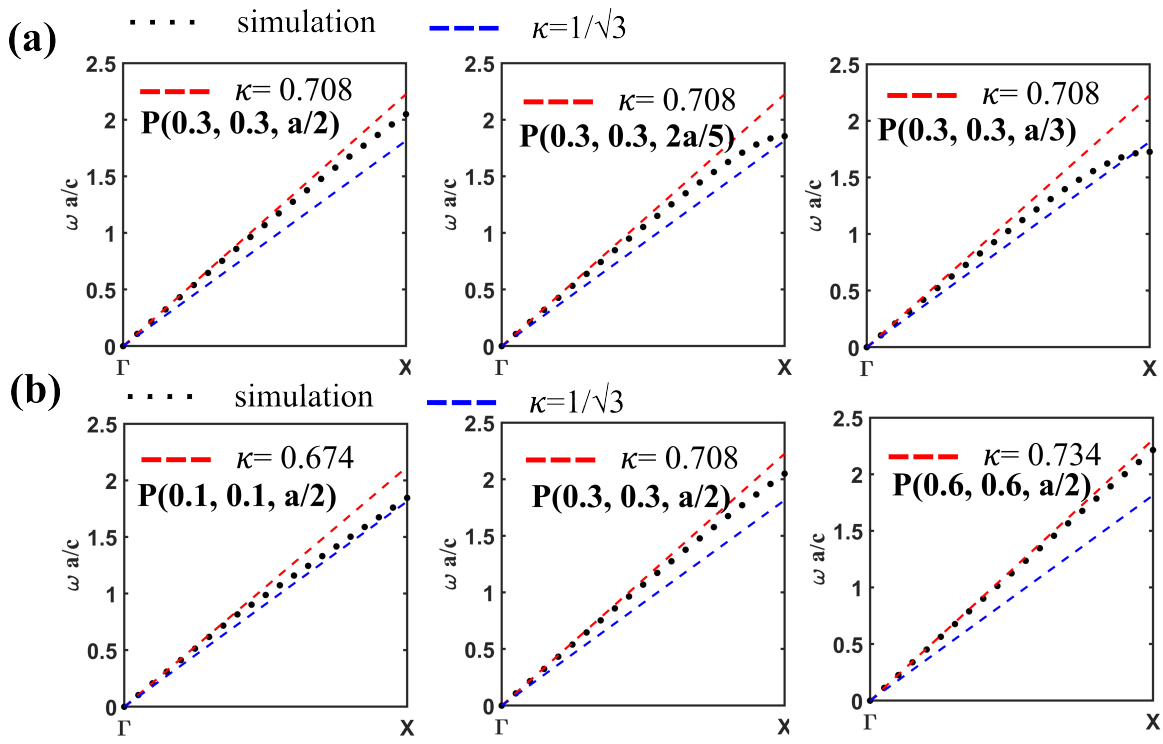

Fig. S3: (a) the corresponding band structures of DNMs with fixed radius of r = 0.3 mm and varying relative distance R = a/2(1, 1, 1), 2a/5(1, 1, 1), and a/3(1, 1, 1); (b) bandstructures of DNMs with a fixed offset of a/2(1, 1, 1) of two identical wire meshes. The radii are 0.1, 0.3 and 0.6 mm, respectively; Black dots are full-wave simulations, blue dash lines show the $\frac{1}{\sqrt{(3)}}$ slop and the red dash lines are the results from HDP model

DNM parameters, such as the radius of the metal wires and the relative offset between the two nets. This assumption has been confirmed through simulations of DNMs with various parameters, as shown in Fig. S3 and discussed in Sec. (S2). In the limit of small radii, the dispersion of fundamental EAW modes in DNMs can be approximated as

$$\omega_a \gtrapprox \frac{1}{\sqrt{3}} k_a c, \tag{S26}$$

To summarize, the EAW modes in DNMs are characterized by a quasi-longitudinal nature and an exact dispersion relationship that only weakly depends on the particular geometrical parameters.

S2 Bandstructure of DNMs with different parameters

DNMs were homogenized using an HDP model in Sec. (S1.4). We showed that the EAW mode in DNMs can be represented by two species of charged particles moving in opposite directions. Using this model, we derived an exact dispersion relation Eq. (S1.3) in the long wavelength limit. The dispersion relation mainly depends on the average pressure parameter of the two networks, which is $\kappa \gtrapprox 1/\sqrt{3}$. To validate this finding, we conducted numerical simulations on DNMs with varying radii (Fig. S3(a) and relative positions (Fig. S3(b).

In Fig. S3(a), we begin with two wire meshes with a fixed relative space offset $a/3(1,1,1)$ and different plasma frequencies tuned by the equal radius of the two wire meshes from 0.02 a, over 0.06 a, to 0.12 a. The corresponding band structures are shown in Fig. S3(b). The black dots are from full wave simulations, while the blue lines show the limiting $\omega/c = \frac{1}{\sqrt{3}}k$ dispersion. As expected, the DNM slope in the vicinity of the Γ-point is larger in all three cases and approaches the limit for small radii. The model is of course invalid when approaching the X-point due to the intrinsic non-homogeneous

and periodic nature of the DNM structures. In Fig. S3 (b), we demonstrate DNMs with various offsets while keeping the plasma frequency of both nets equal and constant (the radius is 0.08 a). The results are again consistent with the theoretical expectation from the HDP model. Upon close inspection, the low-frequency slope approaches the blue limit when the two networks come closer together.

S3 Different double network geometries

While our theory above has been rigorously derived for the pcu double network only, the two main physical features are inherent to the plasmonic double network topology and symmetry rather than the particular geometrical realization. These features are the slope of the EAW band in the low-frequency limit and the longitudinal nature of the homogenized electric field. We here demonstrate that both features are indeed observed for two other known lowest genus double net geometries: the balanced double gyroid (srs-c, $Ia\bar{3}d$ symmetry) and double diamond (dia-c, $Pn\bar{3}m$ symmetry) morphologies (abbreviations as in [58]).

Let us first re-examine the longitudinal nature from a symmetry perspective. In the quasi-static limit, a non-trivial solution to the Poisson equation requires the two nets to be on different potentials [41]. Three situations can generally be distinguished

1. the two nets are only interchanged by one or more space group elements S with point symmetry part that is not the identity[3],
2. the two nets are interchanged by a primitive lattice translation[4],
3. the two nets are no symmetry copy of one another[5].

The cubic examples discussed here all belong to the symmetric cases 1 and 2. In these cases, the square S^2 of the symmetry operation that exchanges nets evidently maps the two nets onto themselves. The potential is, therefore, unchanged by S^2 as the individual nets are short-cut in the quasi-static limit. As a consequence, S yields a multiplication of the potential by -1, and the two nets must hence be on opposite potential. In case 1, the Bloch character is trivial, and the EAW band emanates at zero frequency at the Γ-point. In case 2, the Bloch character is -1 with respect to a primitive lattice translation, and the EAW hence emanates at zero frequency at the corner of the Brillouin zone.

With these preliminary considerations in mind, we first revisit the pcu-c double net. As the pcu-c evidently belongs to case 2 above, with a primitive body-centered cubic lattice translation interchanging nets, the EAW band emanates at zero frequency at the H point [66]. Since H lies along the cubic $\langle 100\rangle$ direction, any state at the center of the surface Brillouin zone (with vanishing lateral $\mathbf{k}$) of a (100) inclined slab is therefore made by a superposition of counter-propagating EAW modes along Γ-H. The behavior in the quasi-static limit now further yields the irreducible representation, or *irrep*, of the electric field with respect to the group of the wave vector [48], which is the C_{4v} point group in this case. Since all elements of C_{4v} do not interchange networks and the individual networks are on constant potential in the quasi-static limit, the EAW irrep is trivial. Therefore, the homogenized field cannot have a component perpendicular to the wave vector direction, as these would transform with a non-trivial 2D E irrep. The fields must be longitudinal from a symmetry perspective over the whole EAW and Langmuir bands, which are glued together and form one band.

The srs-c is of case 1 above, and the EAW band emanates at the Γ-point of the body-centered cubic Brillouin zone at zero frequency. The bandstructure along $\Gamma-H$ ($\mathbf{k}=k\,\mathbf{e}_x$ with $k\in[0,2\pi/a]$) for wire radius of $0.02a$ is shown in Fig. S4 (a). It agrees perfectly with the HDP prediction for the corrected pressure parameter of $\kappa\approx 0.675$ for the wire radius of $0.02a$ over the whole band. This can be understood as follows: The group of the wave vector is again C_{4v}, which is isomorphic to the abstract group G_8^4 in [67]. Considering the quasi-static potentials, the EAW band must be even with respect to the C_{4_2} screw rotation and the C_2 rotation (which maps every single net onto itself) and odd with respect to the glide mirror planes (which interchange networks). It, therefore, has the 1D representation R_2 in G_8^4. At the H point, the EAW joins a 6-fold degenerate point, which transforms according to the R_{14} representation in G_{96}^4, which splits equally into the 4 1D and one

[3] In other words, we have $S=(P|\mathbf{t})$ in Seitz notation with a point symmetry $P\neq\mathbb{1}$ and a translation part $\mathbf{t}$, which might be non-zero (screw axis or glide mirror for example).

[4] $S=(\mathbb{1}|\mathbf{T})$ in Seitz notation, where $\mathbf{T}$ must be a primitive lattice vector.

[5] This case is always possible for unbalanced double nets as, for example, the qtz-qzd double net [65].

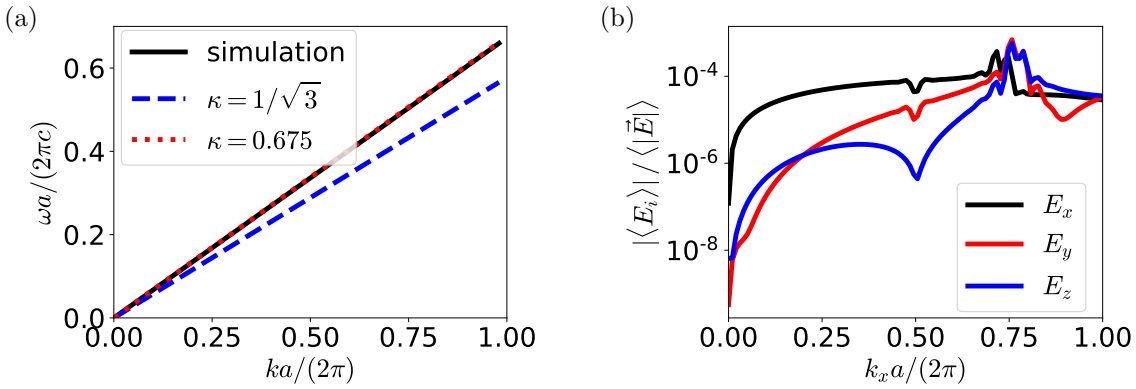

Fig. S4: EAW mode characterization for the srs-c double net along the Γ-H path (parametrized by $\mathbf{k} = k\,\mathbf{e}_x$). (a) Dispersion relation compared to the HDP prediction with limiting ($1/\sqrt{3}$) and radius corrected (0.675) κ. (b) Averaged field components normalized by averaged field intensity parallel to $\mathbf{k}$ ([100]) and along perpendicular high symmetry directions.

2D representations along Γ-H: $R_{14}(G_{96}^4) = \sum_{i=1}^{5} R_i(G_8^4)$. This allows the R_2 representation to form a pair with its time reversal symmetric R_4 representation to form a back-folding at H with finite and opposite slopes of the two bands. As in the pcu-c scenario, the longitudinal EAW behavior is protected by symmetry. Since the group of the wave vector contains a C_{4_2} screw axis and diagonal glide mirrors that both contain a shift along the propagation direction, only the non-symmorphic wallpaper subgroup $p2gg$ (number 8 in [69], with isogonal C_{2v} point group, can be employed to make a general prediction regarding the homogenized fields. Considering the quasi-static potentials again, we obtain an even symmetry classification with respect to the C_2 symmetry in $p2gg$. This classification evidently does not permit homogeneous field components perpendicular to the direction of the wave vector. The odd symmetry behavior with respect to the glide mirror symmetry in $p2gg$, on the other hand, prohibits a homogenized field component along $\mathbf{k}$. For the srs-c, we, therefore, expect a truly vanishing homogenized electric field that extends over the whole EAW band. This vanishing field is demonstrated in Fig. S4 (b) within the numerical precision of the simulations (note the logarithmic y-axis).

Similar to the pcu-c, the dia-c network with simple cubic $Pn\bar{3}m$ symmetry belongs to case 2 above. The EAW band, therefore, emanates at the simple cubic R-point [67]. Consequently, the EAW band lies outside of the light cone along the cubic ⟨100⟩ and ⟨110⟩ directions and cannot lead to BICs. For a slab with (111) inclination, however, the EAW band along the path connecting R with Γ ($\mathbf{k} = (\frac{\sqrt{3}\pi}{a} - k)\frac{1}{\sqrt{3}}(1,1,1)^\intercal$ with $k \in [0, \frac{\sqrt{3}\pi}{a}]$) lies at the center of the surface Brillouin zone. The low-frequency dispersion agrees again perfectly with the HDP prediction with corrected $\kappa \approx 0.675$ as shown in Fig. S5 (a). It, therefore, yields BICs by the same mechanism as exploited in the pcu-c case with slab inclination of (100), assuming a longitudinal homogenized electric field. Such a field is guaranteed by the trivial symmetry classification of the mode with respect to the C_{3v} group of the wave vector[6], which only allows a homogenized field parallel to $\mathbf{k}$. This longitudinal nature is once again demonstrated through full-wave simulations in Fig. S5 (b).

S4 Analytical quasi-BICs and transmission spectra

We here derive an analytical model that reveals the connection between the EAW bulk picture and the slab modes. It generates a good prediction for the quasi-BIC modes and the transmission spectra. Let us first solve the scattering problem using two counter-propagating EAW slab modes only. We first define the two vacuum domains I and III, semi-infinite in z-direction and infinite in x and y, and the DNM slab domain II. As the electromagnetic fields vanish in the HDP model, we need to extract fields at the domain interfaces from the simulations. The EAW fields in the DNM exhibit longitudinal

[6] Even though $Pn\bar{3}m$ is non-symmorphic, the elements of the group of the wave vector (labelled 1, 5, 9, 38, 43 and 48 in [68] are pure mirrors and rotations through the crystallographic origin.

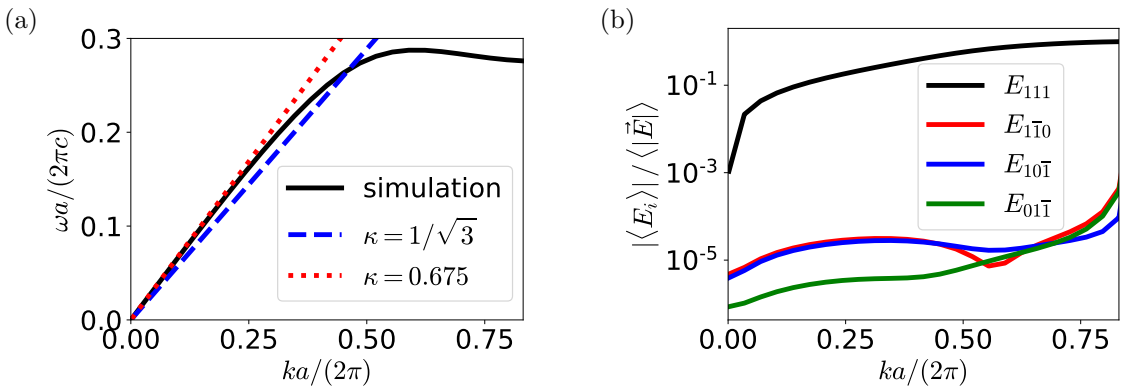

Fig. S5: EAW mode characterization for the dia-c double net along the R-Γ path (parametrized by $\mathbf{k} = (\frac{\sqrt{3}\pi}{a} - k)\frac{1}{\sqrt{3}}(1,1,1)^\intercal$). (a) Dispersion relation compared to the HDP prediction with limiting $(1/\sqrt{3})$ and radius corrected (0.675) κ. (b) Averaged field components normalized by averaged field intensity parallel to $\mathbf{k}$ ([111]) and along perpendicular high symmetry directions.

electric fields and vanishing magnetic fields, as evident from Eq. (S25) and Fig. 2(a) in the main text. To solve the homogenized Maxwell equations (which is equivalent to cutting the Rayleigh series at the fundamental Bragg order) at the slab surface, however, we need to average the fields over this surface rather than the whole unit cell [57]. Considering an in-plane wave vector q along the x direction, we obtain a homogenized electric field pointing along x and a magnetic field pointing along y. This behavior is consistent with the symmetry classification for the mirror-symmetric DNM and means that the EAWs only couple to p polarized waves in the vacuum domains. One further obtains that the surface impedance $Z := E_x/H_y$ is largely independent of the frequency and, consistent with optical reciprocity, quadratically depending on q in good approximation. For an EAW wave propagating in positive z direction, we obtain

$$Z_2 \approx 2.5 \left(\frac{qa}{2\pi}\right)^2 .$$

The vacuum impedance, in contrast, is frequency dependent and finite at vanishing q, with

$$Z_1 = \sqrt{1 - \left(\frac{cq}{\omega}\right)^2}$$

for a wave propagating in positive z direction.

We assume a slab of thickness $d = Na$ and the wave numbers in propagation direction are in vacuum $k_1 := \sqrt{(\omega/c)^2 - q^2}$, and in the slab $k_2 := \sqrt{[\omega/(\kappa c)]^2 - q^2}$, using Eq. (S1.3) for equal wire thickness of $0.08a$ ($\kappa \approx 0.72$). The non-vanishing field components for the scattering problem can thus be expressed as

$$H_\mathrm{I} = \left(e^{\imath k_1 (z+d/2)} + r e^{-\imath k_1 (z+d/2)}\right) e^{\imath q x} , \tag{S27a}$$

$$E_\mathrm{I} = Z_1 \left(e^{\imath k_1 (z+d/2)} - r e^{-\imath k_1 (z+d/2)}\right) e^{\imath q x} , \tag{S27b}$$

$$H_\mathrm{II} = \left(A e^{\imath k_2 z} + B e^{-\imath k_2 z}\right) e^{\imath q x} , \tag{S27c}$$

$$E_\mathrm{II} = Z_2 \left(A e^{\imath k_2 z} - B e^{-\imath k_2 z}\right) e^{\imath q x} , \tag{S27d}$$

$$H_\mathrm{III} = t e^{\imath k_1 (z-d/2)} e^{\imath q x} , \tag{S27e}$$

$$E_\mathrm{III} = Z_1 t e^{\imath k_1 z} e^{\imath q x} . \tag{S27f}$$

$$\tag{S27g}$$

The homogenized Maxwell equations are satisfied if the fields match at both interfaces at $z = \pm d/2$,

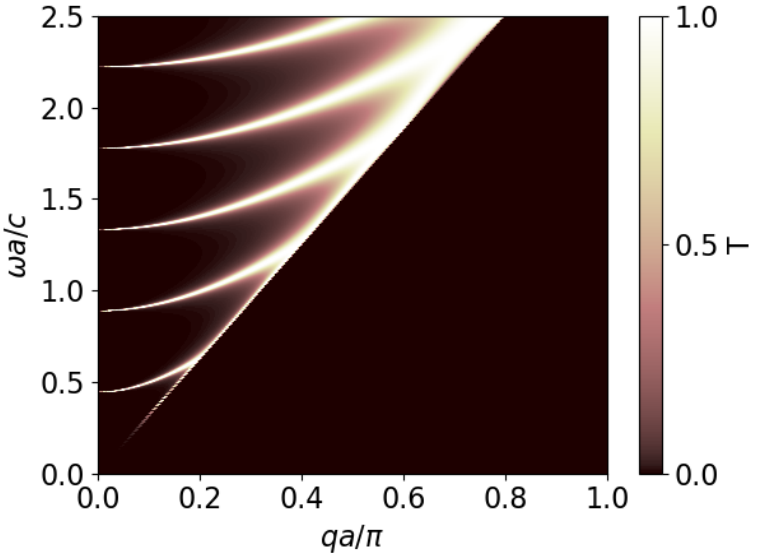

Fig. S6: Analytical transmissivity through an $N=5$ DNM slab using the HDP dispersion Eq. (S1.3) and a homogenized DNM impedance.

yielding a standard scattering problem

$$\begin{pmatrix} Z_1 & 0 & Z_2 p_2 & -Z_2/p_2 \\ 0 & -Z_1 & Z_2/p_2 & -Z_2 p_2 \\ -1 & 0 & p_2 & 1/p_2 \\ 0 & -1 & 1/p_2 & p_2 \end{pmatrix} \begin{pmatrix} r \\ t \\ A \\ B \end{pmatrix} = \begin{pmatrix} Z_1 \\ 0 \\ 1 \\ 0 \end{pmatrix}, \tag{S28}$$

with $p_2 := \exp\{-\imath k_2 d/2\}$. The resulting transmissivity $T = |t|^2$ is shown in Fig. S6. It agrees well with the numerical full wave results in Fig. 3 (d) in the main manuscript, except for a small region close to the light line. Here, the transmission is overestimated significantly as the surface field homogenization breaks down, particularly at large frequencies.

The same fundamental idea can be employed to calculate the quasi-BIC bands. For this, we consider only outgoing waves in the vacuum domains, which transport energy away from the slab, that is, with $\Re\{k_1\}<0$ [>0] in region I [III]. We can characterize the quasi-normal modes as even or odd regarding the $z \mapsto -z$ mirror symmetry of the homogenized slab, substantially reducing the complexity of the problem. In particular, one only needs to consider the fields in one vacuum domain and the even or odd superposition of EAW modes in the slab. The fields are thus expressed by

$$H_{\mathrm{I}} = A e^{-\imath k_1 (z+d/2)} e^{\imath q x} , \tag{S29a}$$

$$E_{\mathrm{I}} = -Z_1 e^{-\imath k_1 (z+d/2)} e^{\imath q x} , \tag{S29b}$$

$$H_{\mathrm{II}} = \left(e^{\imath k_2 z} \pm e^{-\imath k_2 z}\right) e^{\imath q x} , \tag{S29c}$$

$$E_{\mathrm{II}} = Z_2 \left(e^{\imath k_2 z} \mp e^{-\imath k_2 z}\right) e^{\imath q x} . \tag{S29d}$$

For convenience, we have here normalized the eigensolutions such that the positive EAW wave in the slab carries a coefficient of 1. The matching conditions at the slab surface thus yield

$$A = p_2 \pm \frac{1}{p_2} \tag{S30a}$$

$$-Z_1 A = Z_2 \left(p_2 \mp \frac{1}{p_2}\right) . \tag{S30b}$$

At the Γ-point ($q=0$), we immediately obtain $A=0$ from Eq. (S30b). This implies a modal solution with a vanishing homogenized field outside of the slab and thus an infinite quality factor, in

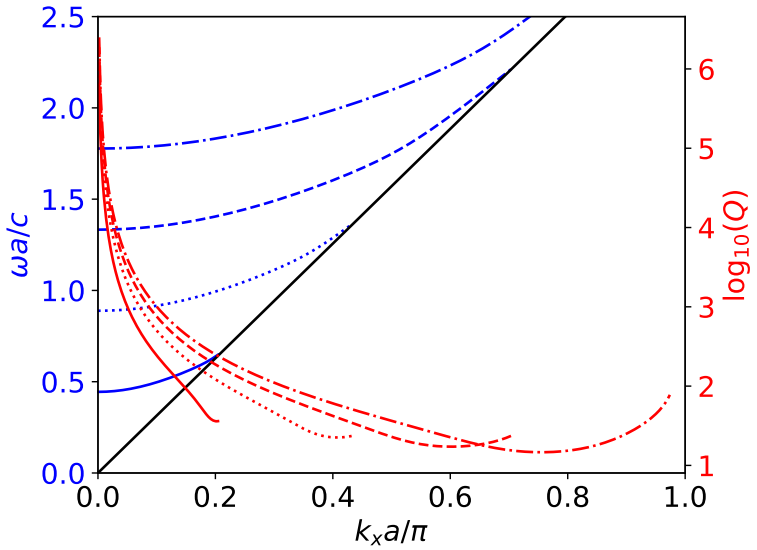

Fig. S7: Bandstructure and quality factor of the quasi-BIC bands for a $N=5$ DNM slab using the HDP dispersion Eq. (S1.3) and a homogenized DNM impedance.

other words, BICs. Eq. (S30a) further yields $p_2^2 = \mp 1$, which reproduces the BIC frequencies obtained from the HDP model under hard wall boundary conditions, that is,

$$\frac{\omega a}{c} = \frac{\kappa \pi n}{N} \quad (n \in \mathbb{N}) \ .$$

For arbitrary q, Eq. (S30a) and Eq. (S30b) yield a finite A and are transcendental in the complex frequency. They, therefore, need to be solved numerically. We divide Eq. (S30b) by $Z_1 \neq 0$ and add it to Eq. (S30a) to obtain

$$f(\omega) := (Z_1 + Z_2)\, p_2 \pm (Z_1 - Z_2)\, /p_2 = 0 \ .$$

Since $f(\omega)$ is holomorphic, except when crossing the light line, we employ a standard Newton method using ω_n as starting guess for $q_{n+1} = q_n + \delta q$ $(n \in \mathbb{N})$ to obtain the quasi-BIC bands and corresponding quality factors $Q := \Re\{\omega\}/(2\Im\{\omega\})$ in Fig. S7. As expected, the bandstructure and quality factors predict the position and width of the transmission bands in Fig. S6, respectively.

S5 Lifting BICs by breaking local symmetry

Throughout this work, we have considered the metals constituting the DNMs as perfect electric conductors so that surface currents flow on the metallic wires and determine the microscopic electromagnetic modes. We have shown in Sec. (S5) that the surface current density forms two quadrupole-like distributions, which are robust against global symmetry breaking. These quadrupole currents are in the 1D representation of the C_{4v} point group labeled B_1 in [48], and thus cannot couple to vacuum radiation, which is in the 2D E representation. However, the BICs can be destroyed by breaking the local C_{4v} symmetry of the individual nets in the DNM. We demonstrate this by introducing an thick metal cylinder segment on the lateral wires along the x and y directions normal to the slab direction z (Fig. S8(a)). These additional cylinders are arranged in such a way that the C_{4v} symmetry is reduced to a single mirror plane on the $x-y$ diagonal. For simplicity, we leave the other net unperturbed. The broken local symmetry, reduced to merely a mirror group, enables couplings of the EAW mode to vacuum modes. When compared to the DNM with two identical unperturbed wire meshes, the slab formed by the perturbed DNM (Fig. S8(c)) degrades the BIC modes at the Γ-point to quasi-BICs with finite Q-factors (Fig. S8(d)). It is, however, worth noting that the perturbed DNM slab can still be well described by the HDP theory, as illustrated by the bulk bandstructure along the out-of-plane z direction in Fig. S8(b), which retains the typical EAW band.

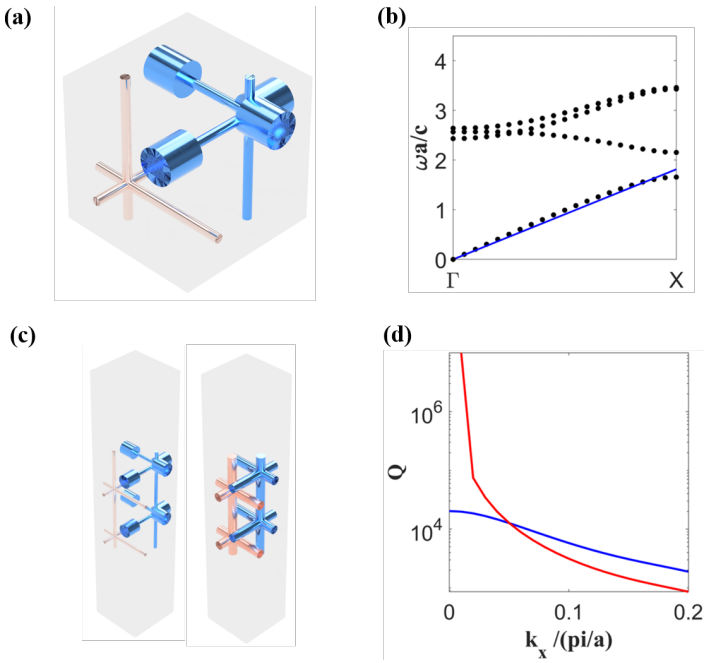

Fig. S8: (a) Schematic diagram of a DMN with broken local C_{4v} symmetry; the radius of the added thick metal cylinder is $0.12a$, while the radius of the unperturbed net is $0.02a$. (b) Corresponding dispersion relation of (a); the black dots are from a full wave simulation, the blue line is the $1/\sqrt{3}$ slope. (c) DMN slab with (left) and without (right) breaking the local symmetry. (d) Q-factor of the nets shown in (c). The Q-factor diverges at the Γ-point for the unperturbed network (red line), which is indicative of the existence of BICs. In contrast, the Q-factor stays finite for the network with strong local symmetry breaking (blue), showing quasi-BIC behavior only.

On the other hand, the nature of the quasi-BICs necessarily imposes changes in polarization structure in the far field. Compared with the 'star' polarization pattern of the BICs in the unperturbed structure (Fig. S9(a)), the perturbed DNM slab exhibits a richer polarization distribution, forming two patches of elliptically polarized states with opposite handedness, separated by a diagonal linear polarization line (Fig. S9(c)). The position of this line on the diagonal is evident from the fact that the in-plane components of both the dominating longitudinal currents and the quadrupole currents are even with respect to the remaining mirror if the mirror coincides with the plane of incidence, that is if the wave vector is invariant. Thus, the far field must obey the same symmetry classification, that is, it must be p polarized, with the electric field confined to the plane of incidence. In all other directions, the EAW field is a combination of even (quadrupole currents) and odd (in-plane longitudinal currents) contributions, and thus the far field is generally elliptically polarized.

The mirror plane divides the $x-y$ plane into two half-planes of opposite elliptical polarizations, which is immediately evident from the action of mirror symmetry σ_d on the modes on one half-plane. The vortex at the origin splits into two circular polarization points on either side. This mechanism is similar to the one reported in [7]; it is of topological origin. The appearance of the circular polarization points becomes evident from tracing the polarization on various momentum space circles of different radii centered around the Γ-point (Fig. S9(c)). The polarization path projected on the Poincaré sphere goes twice through the linear polarization state on the mirror plane. It unfolds from a small figure-of-eight (turquoise, small radius) towards a double-loop around the equator (gray, large radius). It thus necessarily passes through the north/south poles (Fig. S9(d)).

Fig. S9 further indicates that the circularly polarized points lie on the axis perpendicular to the remaining mirror plane. We can understand this behavior from a symmetry perspective. Consider the action of the time-reversal operator τ, which transforms the slab mode with wave vector $\mathbf{k}_\parallel$ into one with $-\mathbf{k}_\parallel$ and complex conjugated field, that is $\tau\mathbf{E}_{\mathbf{k}_\parallel} = \mathbf{E}^*_{-\mathbf{k}_\parallel}$. On the other hand, the mirror symmetry interchanges the field's x and y components and maps $\mathbf{k}_\parallel$ to its negative on the line perpendicular to the mirror plane. The combined operation $\tau\sigma_d$ thus leaves $\mathbf{k}_\parallel$ invariant on this

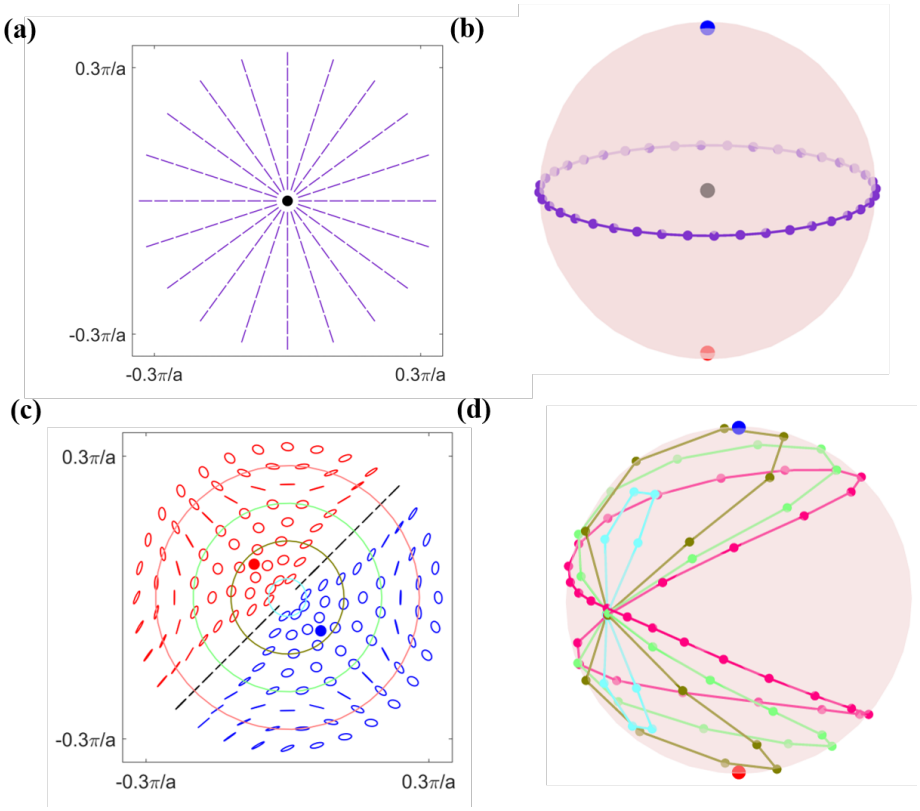

Fig. S9: (a) 2D far-field polarization pattern of BICs in DNMs. (b) Polarization along a circle in (a), projected onto the Poincaré sphere. (c) Far-field polarization pattern of the quasi-BIC for the perturbed DNM. (d) Polarization projected onto the Poincaré sphere along the circles shown in (c).

line. We thus obtain $E_x \overset{!}{=} E_y^*$, so that the normalized in-plane electric far-field depends on one free parameter φ only,

$$\mathbf{E}_\parallel = \frac{1}{\sqrt{2}} \begin{pmatrix} e^{\imath\varphi} \\ e^{-\imath\varphi} \end{pmatrix} .$$

In other words, the field stays on a line of constant longitude on the Poincaré sphere, connecting linear polarization along the mirror plane ($\varphi = 0$ at Γ) and perpendicular to it ($\varphi = \pm\pi/2$ far away from Γ). It must therefore pass the circularly polarized poles ($\varphi = \pm\pi/4$) on either side of the mirror plane.

S6 Quadrupole-like currents in DNMs with different parameters

The surface current densities of the two nets in DNMs parallel to the propagation direction, with opposite signs, resulting in a vanishing homogenized electromagnetic field when approaching the Γ-point, as shown in Fig. 2 in the main text. Meanwhile, small currents flow in the wires oriented perpendicularly to the propagation direction, which we refer to as x w.l.o.g., at finite frequencies. The pcu-c DNM with body-centered cubic symmetry has a global C_{4v} symmetry through the center of each wire. Since the currents in the x wires are constant along the wire surface, they transform trivially under the corresponding C_{4v} symmetry. Consequently, the weak EAW currents in the wires in the y-z plane must transform trivially as well, and therefore either all flow towards the nodes or away from them in a 4-fold quadrupole-like fashion. This expected behavior is demonstrated through the surface current densities obtained from full wave simulations, whose y component is shown in Fig. S10 (a) and the z component in Fig. S10 (d).

Notably, the in-plane geometry of the individual nets dominates the electromagnetic distribution since the currents on the two nets experience very weak inter-coupling at low frequencies. The local

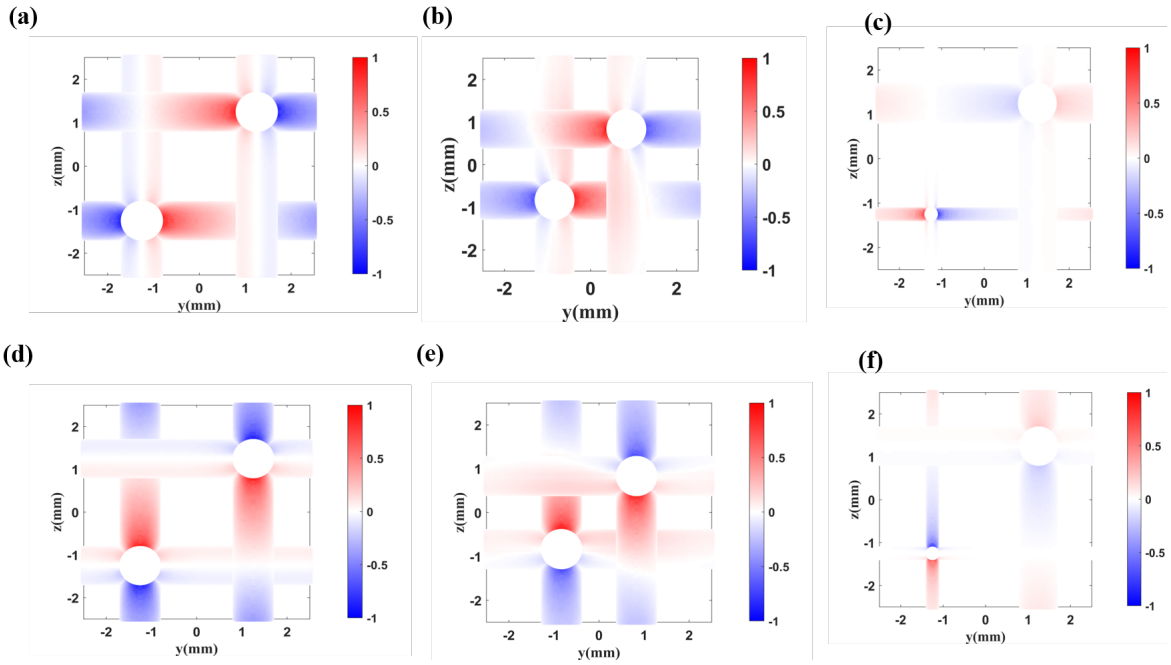

Fig. S10: y and z components of surface current densities J_s of DMNs with different parameters near the static limit at $k_x = 0.05\frac{\pi}{a}$ and $k_y = k_z = 0$. (a), (b)and (c) show the J_{sy} distribution, while (b), (d), and (f) show J_{sz}. DNM parameters for (a) and (d) are (0.08 ,0.08 ,0.5); for (b) and (e) (0.08 ,0.08 ,0.33); for (c) and (f) (0.08 ,0.02 ,0.5).

C_{4v} symmetry of every single net thus guarantees the formation of the aforementioned quadrupole-like current distributions, even in the absence of a global C_{4v} symmetry. We demonstrate this behavior through the current distributions shown in Fig. S10 (b) and (e) for DNMs with a non-symmetric shift and in Fig. S10 (c) and (f) for distinct wire radii. To a very good approximation, these fields retain their trivial character with respect to the individual net's C_{4v} symmetry.

Importantly, this trivial character is evidently incompatible with the free space photon modes, which carry the non-trivial character of the $E_{\pm}$ (right and left circular polarization) irreducible representation [38].

S7 EAWs BICs in real Metallic DNMs

In this supplementary section, we present additional simulations that account for the impact of metal losses on Electron Acoustic Wave (EAW) quasi-Bound States in the Continuum (BICs).

To conduct our simulations, we utilized copper as the material due to its widespread usage and cost-effectiveness in practical applications. Copper has a known conductance of $5.96 \times 10^7 S/m$ at mircowave frequencies, making it a suitable choice for our investigations.

Our study considered two configurations: DMN slabs and sub-wavelength DMN resonators. The DMN slab parameters were derived from Figure 2(c), with P=(0.4, 0.4, a/2), and for simplicity, we set N=5. By illuminating one side with a plane wave, we observed the reflectivity at various angles (wave vectors k). In the lossless scenario, where the constituent metals can be approximated as a perfect electric conductor (PEC),Fig. S11 (a) displays the square of reflectivity (indicating power) for the fourth band branch. The frequencies associated with this branch are approximately 16.3 GHz at different wave vectors (small k) in the lossless case. As the wave vector (incident angle) decreases, the half bandwidth narrows. Notably, under normal incident conditions, BICs emerge without coupling to the surrounding environment.

To assess the impact of metal losses, we performed simulations considering the conductive properties of copper. Fig. S11 (b) demonstrates the square of the reflectivity curve in the presence of losses. As expected, the half bandwidth of the indicating power curve narrows as the wave vector (k vector)

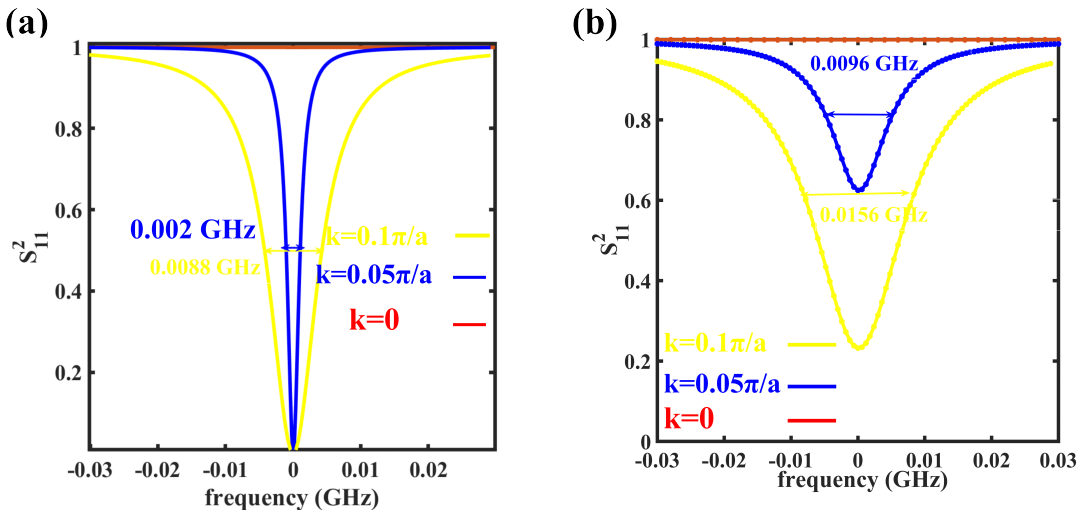

Fig. S11: (a) lossless DMNs and (b) lossy DMNs; The plot showcase the square of S_{11} parameter (reflectivity) indicating power in the function with frequency. Different wave vectors (k), also depicted using distinct colors (yellow, blue, and red), representing $k = 0.1\pi/a$, $k = 0.05\pi/a$, and $k = 0$, respectively.

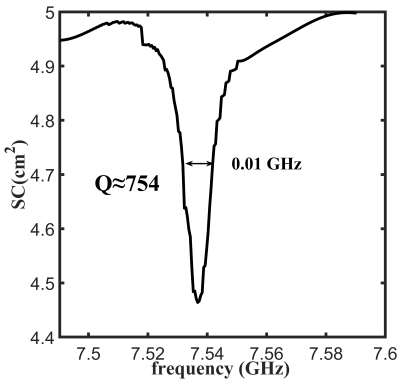

Fig. S12: Scattering cross section in lossy cubic DMNs resonators

decreases, ultimately converging to the Q-factor of the intrinsic resonator mode. Remarkably, even with the presence of losses, bound states in the continuum (BICs) persist when the wave vector (k) equals 0, highlighting their robustness against metal losses.

Importantly, our design was at 10 GHz. range, where metal losses are relatively large. It should be noted that DMNs can be scaled up to larger lattice constant, resulting lower resonance frequencies where metal losses are considerably lower.

In addition to our investigation of DMN slabs, we also studied quasi-BIC resonances in a loss cubic DMN micro-resonator. Our simulation, as shown in Fig. S12, reveals a slightly asymmetric Fano resonance dip in the scattering cross section (SC) at the fundamental quasi-BIC mode, occurring at a frequency of 7.54 GHz. Remarkably, this resonance exhibits a high Q-factor of 750, considering a cube's edge length of 12.5 mm. Similar to the slab configuration, the quasi-BIC states in the cubic micro-resonator manifest themselves as resonances in the scattering cross sections. It is worth noting that the physical size of this resonator is extremely small, on the order of a few unit cells. This characteristic stands in stark contrast to previously reported quasi-BIC resonators that were purely dielectric in nature.

Overall, our results indicate that EAW quasi-BICs hold promise for various technological advancements, even in the presence of metal losses. The demonstrated robustness and high Q-factor make them a compelling option for applications in diverse fields.